









Propagating and Stationary Bright Knots in the Quiet Sun

Jun Zhang¹ , Yijun Hou² , Yue Fang¹, Feng Chen³ , Ting Li² , Xiaoli Yan⁴ , Tao Ding¹, Zhiping Song¹,
Yongyuan Xiang⁴ , and Zhong Liu⁴

¹ School of Physics and Optoelectronics Engineering, Anhui University, Hefei 230601, People's Republic of China; zjun@ahu.edu.cn

² National Astronomical Observatories, Chinese Academy of Sciences, Beijing 100101, People's Republic of China; yijunhou@nao.cas.cn

³ School of Astronomy and Space Science, Nanjing University, Nanjing 210023, People's Republic of China

⁴ Yunnan Observatories, Chinese Academy of Sciences, Kunming 650216, People's Republic of China

Received 2022 September 2; revised 2022 December 4; accepted 2022 December 6; published 2022 December 27

Abstract

The question of what heats the solar chromosphere and corona remains one of the most important puzzles in solar physics and astrophysics. Up to now, two mechanisms are considered to work in heating the chromosphere and corona: magnetic reconnection and wave (turbulent flow) dissipation. But it is still not understood which mechanism is dominant. To solve the heating problem, one important topic at this stage is that we should understand how much energy is contributing from the two mechanisms respectively to the heating. In the quiet Sun, the thermal energy signal is observed as brightenings. Here we report two kinds of bright knots with a total of 3605 in the chromosphere of the quiet Sun, using the data from the New Vacuum Solar Telescope at Yunnan Observatories. The first kind of 1537 bright knots, which is first detected in chromospheric fibrils where waves and their dissipation are ubiquitous, propagates along these fibrils with velocities from 5 to 69 km s⁻¹. The second kind of 2068 knots keeps stationary, and always appears at the footpoints of these fibrils where network magnetic fields exist, suggesting that magnetic reconnection locally produces these stationary knots. Based on the observations of thousands of bright knots, we display the different distribution patterns of the two kinds of bright knots in the quiet Sun, and deduce that half of the energy for heating the chromosphere is supplied by wave dissipation, and the other half by magnetic reconnection.

Key words: Quiet solar corona – Solar extreme ultraviolet emission – Solar magnetic fields – Solar chromospheric heating

Supporting material: animations

1. Introduction

The heating process in the solar atmosphere is still an unresolved problem. The mass and energy flows pass through the solar chromosphere to heat the upper atmosphere (Aschwanden et al. 2007). In the footpoint regions of chromospheric and coronal loops, a much stronger heating rate is believed to be intermittently occurring. In the quiet Sun, a popular activity is bright points (BPs). BPs were first discovered as pointlike bright features in X-ray images (Vaiana et al. 1973), and interpreted as signatures of micro- or nanoflares occurring at the transition region or coronal temperatures. Magnetic flux emergence and cancellation are relevant to these BPs (Priest et al. 1994), suggesting that the BP phenomenon is a consequence of magnetic reconnection. Magnetic reconnection between opposite-polarity field lines would release magnetic energy violently, and contributes to heating the atmosphere. This idea was followed by a large number of studies (e.g., Solanki et al. 2003; Shibata et al. 2007). Theoretical model argues that an X-point magnetic reconnection locally heats the corona and produces BPs (Priest et al. 1994). Recent EUV observations (174 Å) have revealed “campfires” in the quiet Sun corona, with length scales between 40 and 4000 km and durations between 10 and 200 s (Berghmans et al. 2021). These campfires sometimes exhibit propagating signatures along small loop-like structures

(Mandal et al. 2021), with speeds between 25 and 60 km s⁻¹. It is suggested that a loop-like structure gets heated due to (component) magnetic reconnection, then the heated plasma appears as a campfire (Berghmans et al. 2021; Mandal et al. 2021).

In the solar atmosphere, another ubiquitous activity is magneto-hydrodynamic (MHD) waves. The convection below the solar visible surface and solar global oscillations may produce MHD waves in the photosphere, which then propagate upward into the corona (Tomczyk et al. 2007; Antolin et al. 2017). There are three basic types of MHD waves: slow and fast magnetoacoustic waves, and Alfvén waves. They carry energy, and may play an important role in coronal heating (Taroyan & Erdélyi 2009). To confirm the dynamics of these MHD waves, simulations are usually used. Simulations of transverse waves in coronal loops have revealed that the Kelvin–Helmholtz instability (KHI) occurs near the boundary of loops (Terradas et al. 2008; Magyar et al. 2015). KHI generates turbulent small structures, makes the dissipation of the wave energy much more easier, and heats the chromosphere and corona (Howson et al. 2017).

Many researchers have tried to solve the heating problem, and got the following consensus. The energy heating the atmosphere comes from solar magnetic fields. Magnetic reconnection and wave dissipation transform the magnetic energy and wave energy into thermal energy, which heats the atmosphere. However, there still exist several key issues. For example, does magnetic reconnection or wave dissipation play the dominant role? Do both of them contribute to heating a given atmosphere structure? In this Letter, we study



Original content from this work may be used under the terms of the [Creative Commons Attribution 4.0 licence](https://creativecommons.org/licenses/by/4.0/). Any further distribution of this work must maintain attribution to the author(s) and the title of the work, journal citation and DOI.

chromospheric bright knots using high-resolution $H\alpha$ observations from the 1 m New Vacuum Solar Telescope (NVST; Liu et al. 2014). These bright knots are tracked one by one, and finally 3605 knots are detected. We display the distribution patterns of these bright knots in the quiet Sun, analyze the physical mechanisms of these knots, and discuss whether magnetic reconnection or wave dissipation plays a dominant role for heating the chromospheric atmosphere.

2. Observations and Data Analysis

The NVST with a clear aperture of 985 mm is the primary facility of the Fuxian Solar Observatory, operated by Yunnan Observatories, Chinese Academy of Sciences. The main goals of the NVST are high-resolution imaging and spectral observations. $H\alpha$ 6562.8 Å channel is used to image the dynamic solar chromosphere with high temporospatial resolution. The present study is mainly based on the $H\alpha$ observations in the quiet Sun (N13W10) from 06:48:36 UT to 09:54:27 UT on 2019 September 4. The cadence of the data is 11 s. The field of view (FOV) is $126'' \times 126''$ with the pixel size of $0.''136$. The Level 0 data are first calibrated to Level 1, including dark current subtraction and flat field correction. Then the calibrated Level 1 images are reconstructed to Level 1+ by speckle masking.

We also employ the Atmospheric Imaging Assembly (AIA; Lemen et al. 2012) and Helioseismic and Magnetic Imager (HMI; Scherrer et al. 2012) observations from the Solar Dynamic Observatory (SDO; Pesnell et al. 2012). The SDO/AIA detects uninterruptedly the full disk of the Sun at 10 wavelengths with a 12 (24) s cadence and a $0.''6$ per pixel sampling. The data reflect plasma with different temperatures (from 5000 K to 2.5 MK) from the photosphere to the corona. The SDO/HMI measures the Doppler velocity, line-of-sight (LOS) magnetic field, and vector magnetic field at the photosphere of the Sun. The data cover the full disk of the Sun with a spatial sampling of $0.''5$ per pixel sampling. The full disk LOS magnetograms, used in this Letter, are taken at a cadence of 45 s. The AIA images are calibrated using the standard `aia_prep.pro` routine in SolarSoft (SSW). The AIA and NVST data are coaligned by matching the locations of network bright points observed in both the AIA 304 Å and NVST $H\alpha$ images.

By examining the $H\alpha$ observations, we notice that there are two kinds of bright knots: propagating knots and stationary ones. To ensure no omission or repetition of the bright knots, we track all the knots one by one. First we divide the 3.1 hr observations into six durations, and each duration is about 30 minutes. The images in each duration are divided into four regions, corresponding to four quadrants; then we measure the propagating bright knots in turn from a quadrant to another one in a 30 minute movie. We start to record a bright knot as a real signal when its brightness exceeds more than 5% of the background brightness, and stop recording while the brightness exceeds less than 5%. The duration is considered as the lifetime of the bright knot. Furthermore, the signal should be clearly detected at least in three successive images. As the cadence of the images is 11 s, the lifetime must be longer than 22 s. For each propagating knot, 12 parameters are recorded, including the begin time and the end time, and the begin position and the end position, the peak brightness and its corresponding area, time, and position, the ratio between the peak brightness and background one, the lifetime, the propagating distance, and the

velocity. After finishing the measurement of the propagating bright knots, we start to measure the stationary knots. For each stationary bright knot, eight parameters are recorded, including the begin time and the end time, the peak brightness and its corresponding area, time, and position, the ratio between the peak brightness and background one, and the lifetime.

3. Results

Employing the $H\alpha$ observations near the solar disk center from the NVST on 2019 September 4, we have detected 3605 bright knots in the chromosphere of the quiet Sun. These knots can be classified into two types, based on their kinematic property. The first type of knots (1537) appears in chromospheric fibrils, and propagates along these fibrils. The second one (2068), however, always appears at the footpoints of these fibrils where network magnetic fields exist, and keeps stationary during their lifetimes. Figure 1(a) displays an HMI magnetogram, overlaid with 2068 stationary bright knots. These knots do not distribute uniformly, instead, most of them are located at the stronger network magnetic fields. Three examples of these stationary knots are displayed in Figure 1(b). For the propagating knots, as they propagate along chromospheric fibrils, we overlie all of them on a $H\alpha$ image (Figure 1(c)). To better understand this type of knots, we also display three examples in Figure 1(d) (an animation showing Event 4 evolution is attached).

Thousands of bright knots allow us to obtain some statistical results. For the propagating knots, their lifetimes range from 22 to 208 s, with a peak around 75 s. For the stationary ones, their lifetimes range from 32 to 679 s, with a peak around 255 s (Figure 2(a)). Generally, the stationary knots have both longer lifetimes and a long-span lifetime distribution, compared to the propagating ones. Besides, the propagating ones have one more velocity parameter. The velocities range from 5 to 69 km s^{-1} , with a peak around 16 km s^{-1} (Figure 2(b)). Figure 2(c) displays the frequency distribution as a function of enhanced (background-subtracted) brightness of the stationary bright knots. One can see that in the brightness range of $0.8\text{--}4.0 \times 10^{10}$ DN, the frequency distribution can be fitted by a power-law function with the power-law index (α) of 3.44 ± 0.14 . As for the propagating knots (Figure 2(d)), the frequency distribution in the brightness range of $1.9\text{--}5.4 \times 10^9$ DN can also be fitted by a power-law function with the index of 4.25 ± 0.20 . To assess the power-law fit applied here, we further calculate the chi-square value (χ^2) according to the formula

$$\chi^2 = \sum ((\text{Value}_{\text{expected}} - \text{Value}_{\text{observed}}) / \text{Error}_{\text{observed}})^2,$$

where $\text{Value}_{\text{expected}}$ is a theoretical value of each bin expected from the power-law function, $\text{Value}_{\text{observed}}$ is the actual value of each bin, and $\text{Error}_{\text{observed}}$ is the error of $\text{Value}_{\text{observed}}$. It is revealed that the χ^2 of the power-law fitting for 15 bins in the range of $0.8\text{--}4.0 \times 10^{10}$ DN shown in Figure 2(c) is 13.34, and that for 10 bins in the range of $1.9\text{--}5.4 \times 10^9$ DN shown in Figure 2(d) is 27.57. Both of the χ^2 values indicate a good fitting effect. Here it is worth noting that the $\text{Error}_{\text{observed}}$ is simply estimated from the square root of numbers in each bin, which should be a lower limit value of error. As a result, the χ^2 estimated here could be larger than the true value.

By examining the $H\alpha$ images and AIA 304 and 171 Å observations, as well as HMI LOS magnetograms, we realize

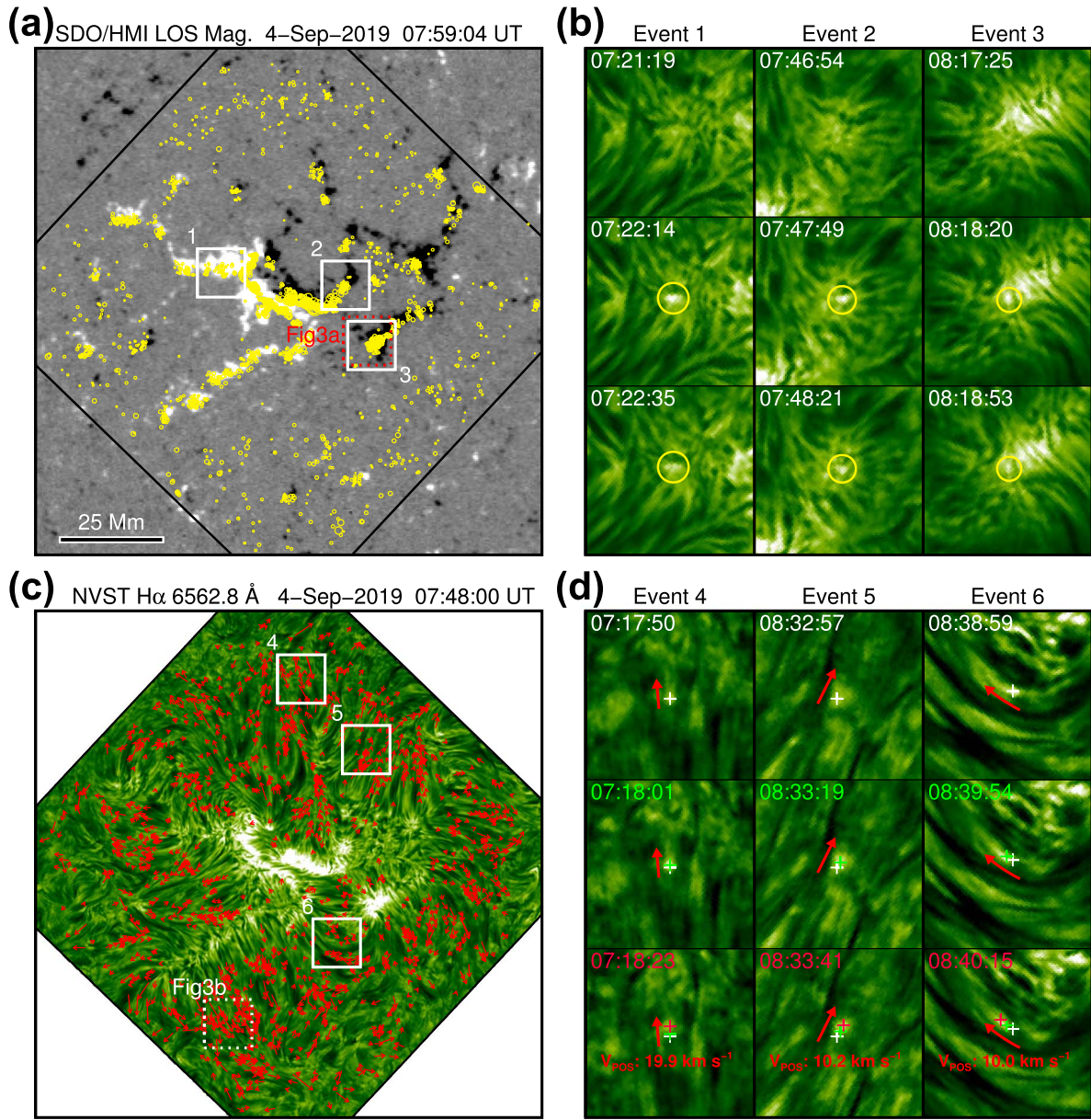


Figure 1. Stationary and propagating bright knots in a quiet Sun region. (a) 2068 stationary bright knots overlaid with a magnetogram. Each circle represents a stationary knot, and the radius of the circle is proportional to the peak brightness. Windows 1–3 outline the FOVs of three events 1–3 displayed in (b), respectively. A dotted line window outlines the FOV of Figure 3(a). (b) Temporal evolution of the three stationary bright knots (windows 1–3 in (a)). (c) 1537 propagating bright knots overlaid with a $H\alpha$ image. Each arrow represents a propagating knot. The arrow direction represents the propagation one, and the arrow length the propagation velocity. Windows 4–6 outline the FOVs of three events 4–6 displayed in (d), respectively. A dotted line window outlines the FOV of Figure 3(b). (d) Temporal evolution of the three propagating bright knots (windows 4–6 in (c)). An animation of $H\alpha$ observations showing Event 4 evolution is available, and the real-time duration of the animation is 1 s.

(An animation of this figure is available.)

that it is very difficult to determine the connection of a chromospheric bright knot to photospheric magnetic field and an AIA EUV brightening. First, the observed target is an enhanced magnetic network region, the radiations of both the 304 and 171 Å wavelengths are strong, and more than 90% of the bright knots are submerged in the strong radiations. Second, the size of the $H\alpha$ bright knots is small ($\sim 0.9 \text{ Mm}^2$), close to the spatial resolution limitations of both AIA and HMI observations. In the area where 304 Å radiation is not much strong, 198 stationary bright knots and 126 propagating knots are detected in the corresponding $H\alpha$ region. Among which, 9 stationary bright knots and 11 propagating knots connect to 304 Å brightenings, as well as 3 stationary bright knots to

photospheric magnetic field evolution. Figure 3(a) displays the temporal evolution of a $H\alpha$ stationary bright knot relevant to photospheric magnetic flux emergence and cancellation. The brightness enhancement of the knot corresponds to the flux decrease of the positive field. Meanwhile, an AIA 304 Å brightness enhancement is corresponding to the $H\alpha$ knot. Figure 3(b) shows the temporal evolution of a $H\alpha$ propagating knot with a velocity of $36.6 \pm 3.8 \text{ km s}^{-1}$. An AIA 304 Å brightness enhancement is also corresponding to this $H\alpha$ bright knot.

Propagating brightening can also be found in coronal loops in a 3D MHD model (Chen et al. 2014). The numerical simulation is conducted with the Pencil code (Brandenburg &

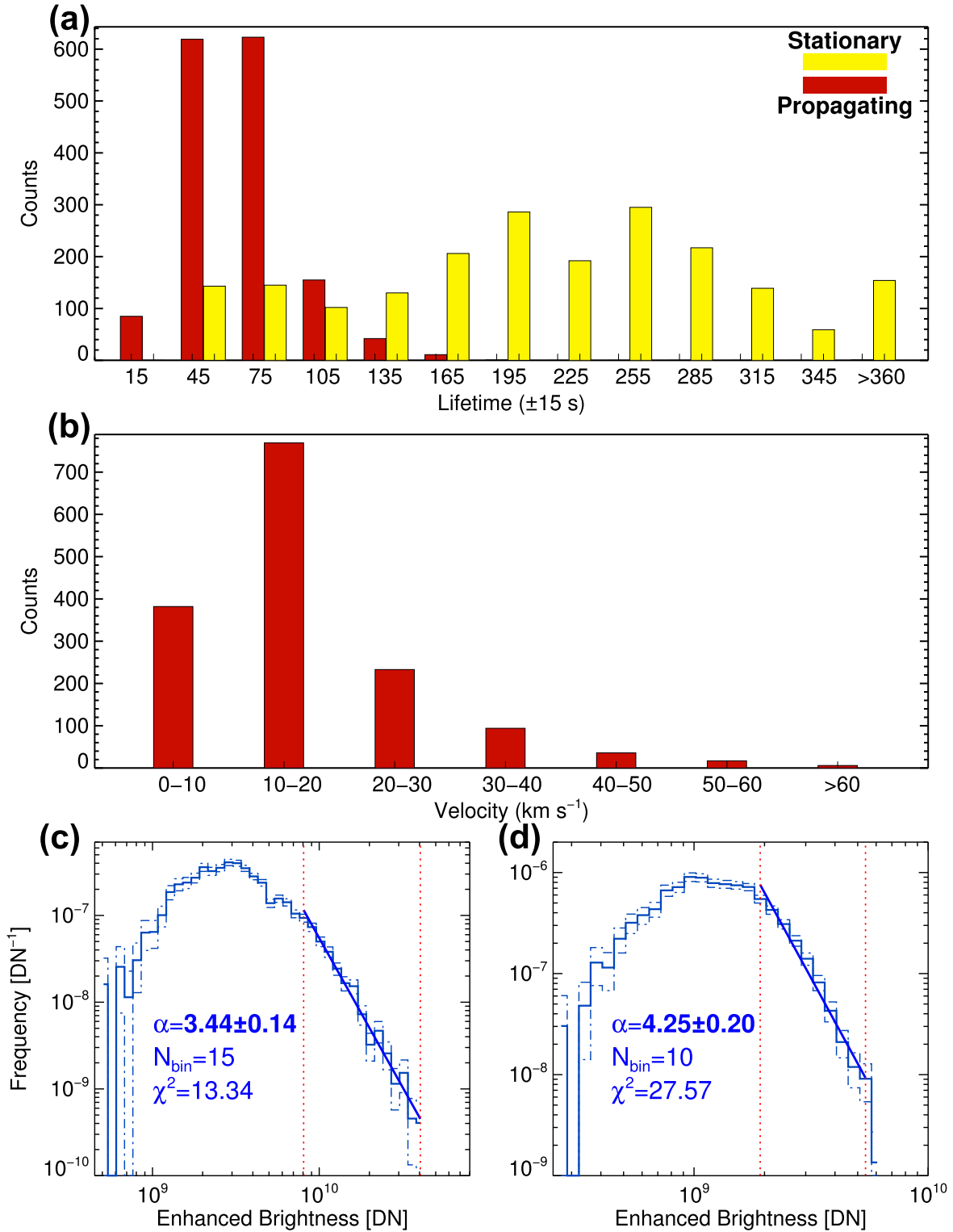


Figure 2. Statistical properties of the stationary and propagating bright knots. (a) Lifetime histograms of the stationary and propagating bright knots, respectively. (b) Velocity histogram of the propagating bright knots. (c) The frequency distribution as a function of enhanced brightness of stationary bright knots. The blue solid histogram showing the frequency distribution is fitted by a simple power-law function in the range from 0.8 to 4.0×10^{10} DN (see the two red dotted lines). The dashed-dotted histograms represent error bars estimated from the square root of numbers in each bin. N_{bin} represents the bin number in the fitting range. The power-law index α is 3.44 ± 0.14 , and the chi-square (χ^2) 13.34. (d) Similar to (c), but for propagating ones. The fitting range indicated by two red dotted lines is from 1.9 to 5.4×10^9 DN.

Dobler 2002). The setup is similar to that of previous works (Bingert & Peter 2011; Chen et al. 2014). A $147.456 \times 73.728 \times 50 \text{ Mm}^3$ domain is resolved by $1024 \times 512 \times 256$ grid points. The grid spacing is constant (144 km) in the

horizontal direction, but changes in the vertical direction smoothly from 30 km in the photosphere to 190 km in the coronal part. The numerical simulation solves a sophisticated energy equation that considers highly anisotropic heat

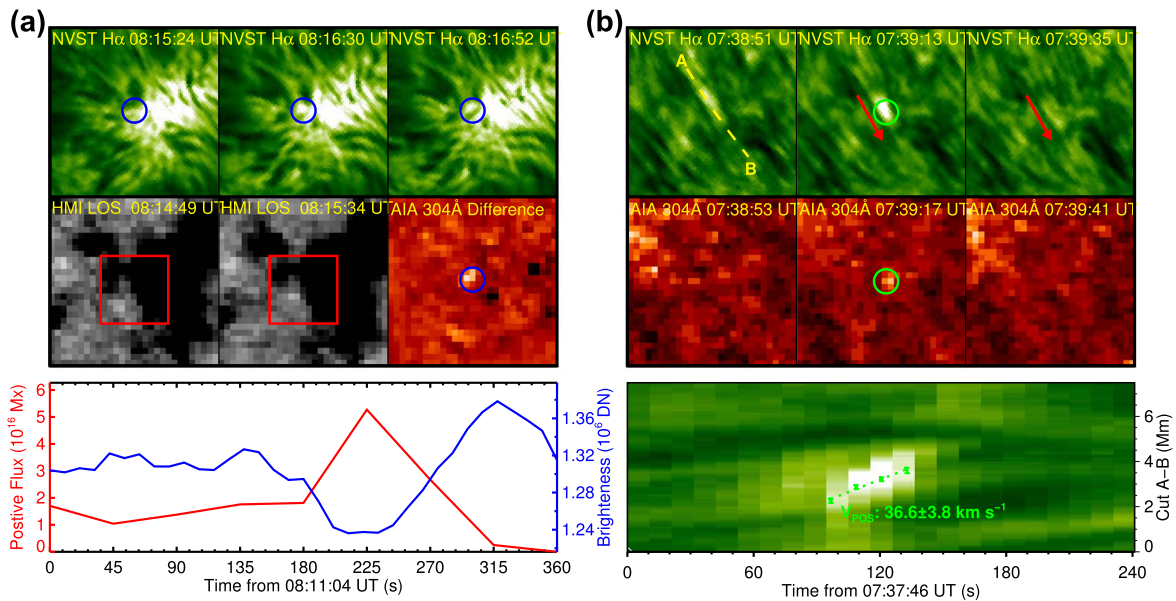


Figure 3. Connection of chromospheric $H\alpha$ bright knots to photospheric magnetic flux evolution and AIA 304 Å brightenings. (a) Temporal evolution of a $H\alpha$ stationary bright knot (top) relevant to photospheric magnetic flux emergence and cancellation (middle). An AIA 304 Å brightness enhancement (middle) is corresponding to the $H\alpha$ bright knot. The positive flux inside the red window (middle) increases from about 1.2×10^{16} to 5.1×10^{16} Mx, then disappears. Meanwhile, the brightness of the knot displayed by the blue curve enhances (bottom). (b) Temporal evolution of a $H\alpha$ propagating bright knot (top) with a velocity of 36.6 ± 3.8 km s $^{-1}$ deduced from a time-distance map (bottom) along Cut A-B (top left). An AIA 304 Å brightness enhancement appears at the same time (middle).

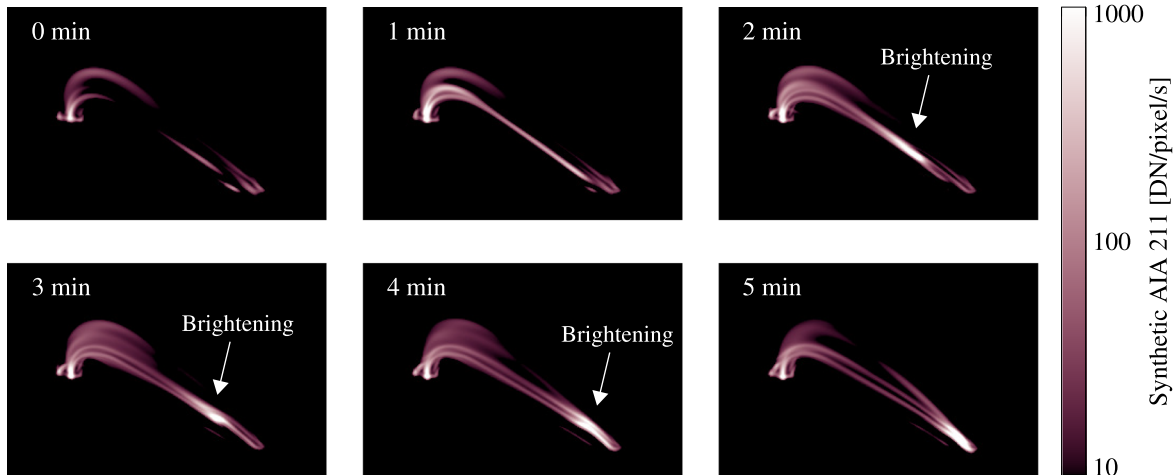


Figure 4. Propagating brightening in coronal loops synthesized from a 3D MHD model. The model corona reproduces EUV observations taken by AIA in the 211 Å channel. It is dominated by emission from Fe XIII showing plasma at around 2 MK. Many bright coronal loops form, but we use a mask to highlight only the loop with the propagating brightening. The distance between the two footpoints of the loop system is about 35 Mm, and the length of the loop is about 45 Mm. The arrows indicate the positions of the brightening. An animation of this figure is available. It runs from 0 to 11.5 minutes in 0.5 minute increments, and the real-time duration of the animation is 4 s. (An animation of this figure is available.)

conductions, optically thin radiative loss, and heating by ohmic dissipation. The bottom boundary of the simulation is placed at the photosphere, where it is coupled with a realistic flux emergence simulation (Rempel & Cheung 2014), such that a time series of physical quantities from the flux emergence simulation is imposed as a time-dependent boundary driver.

Figure 4 displays the synthetic EUV observations taken by AIA in the 211 Å channel with arrows indicating the position of the brightening (an animation is attached). While the main body of the coronal loop is energized by dissipation of the magnetic energy input by field line braiding, a disturbance is triggered by the loop-hosting magnetic field line dynamically emerging into the corona. The leading front of the disturbance coincides with strong localized heating increase, which gives

rise to the propagating brightening. Although the location and temperature of the event in the simulation may differ from the observations shown in this study, it helps to illustrate the scenario that the dissipation of excited propagating disturbances contributes to coronal heating. Surely chromospheric fibrils in numerical simulation would be more helpful to understand the observed one. In the subsequent study, we hope to simulate chromospheric fibrils using the Bifrost code (Gudiksen et al. 2011).

To illustrate the two kinds of bright knots, two schematic drawings are displayed in Figure 5. First, a plasma wave propagates along a $H\alpha$ fibril, then the wave dissipation heats the fibril material, and is observed as propagating brightening (Figure 5(a)). On the other hand, magnetic flux emergence and

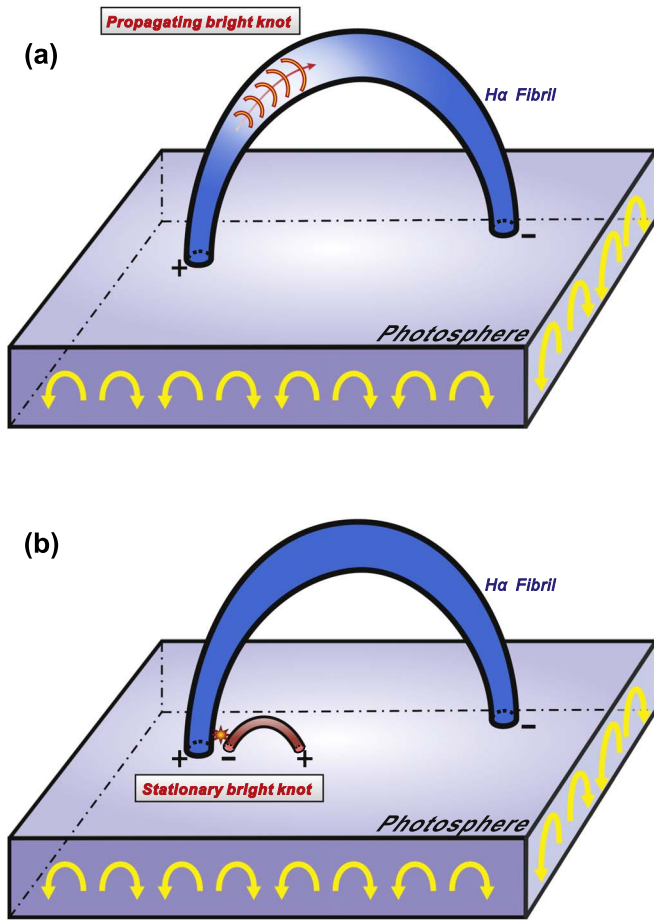


Figure 5. Sketches illustrating the two kinds of bright knots. (a) A plasma wave propagates along a $H\alpha$ fibril at first, then the wave dissipation heats the fibril material, and is observed as a propagating bright knot (see the arcs in the fibril, with an arrow representing the propagating direction). (b) Magnetic flux (the small tube near the left footpoint of the fibril) emergence and subsequently cancellation take place at the footpoint of the fibril, and heat the lower atmosphere; then a stationary bright knot appears (see the red star between the two footpoints of the fibril and the small tube).

subsequently cancellation take place at the footpoint of the fibril and heat the lower atmosphere through magnetic reconnection, and thus stationary brightening appears (Figure 5(b)).

4. Summary and Discussion

In this Letter, we report two kinds of bright knots in the quiet Sun: propagating bright knots and stationary ones. They display different distribution patterns. The propagating bright knots that are first detected in chromospheric fibrils propagate along these fibrils, and the stationary knots always appear at the footpoints of these fibrils.

Waves are ubiquitous in the chromosphere, and propagate from the chromosphere into the corona (De Pontieu et al. 2005). In the solar atmosphere, slow magnetoacoustic waves (SMAWs) have been discovered in magnetic pores (Dorotovič et al. 2014), chromospheric networks (Vecchio et al. 2007), coronal loops (Jess et al. 2016), and polar plumes (Krishna Prasad et al. 2011). SMAWs propagate upwards along the magnetic field lines (Khomenko & Cally 2012), then reach the

coronal heights. Magnetic fields expand in the chromosphere, where different MHD wave modes that are both compressible and incompressible exist (Morton et al. 2012). These waves will make a significant contribution to localized heating. The acoustic wave energy expected to be dissipated in the chromosphere by shock waves is the dominant energy source to heat plage regions (Sobotka et al. 2016; Abbasvand et al. 2020). Upward propagating Alfvén waves increase their amplitude with the expansion of the flux tubes, and generate compressive shock waves, which heat the chromosphere inside the flux tubes (Matsumoto & Suzuki 2012). Heating due to Alfvén wave turbulence is another candidate mechanism suggested for chromospheric heating (Ragot 2019).

The propagating bright knots appear in chromospheric fibrils observed in NVST $H\alpha$ images, and propagate along these fibrils with velocities from 5 to 69 km s⁻¹. To determine which physical mechanism triggering these propagating knots, we examine all the NVST $H\alpha$ observations over the past decade. The examples (Yang et al. 2015; Fang et al. 2022) of unambiguous magnetic reconnection between chromospheric fibrils are no more than 15, implying that magnetic reconnection between fibrils is difficult to occur (or at least difficult to be detected). Besides, all the examples show that magnetic reconnection occurs between fibrils with opposite-polarity fields. Based on photospheric magnetic field observations, we conclude that the magnetic field directions of surrounding fibrils are always parallel to that of these fibrils where propagating knots are detected. We conclude that magnetic reconnection is not a reasonable physical mechanism for triggering the propagating bright knots. On the other hand, waves are ubiquitous in the chromosphere, so wave dissipation will make a significant contribution to localized heating. Furthermore, the speeds of propagating knots are comparable to that of magnetosonic waves (e.g., Ofman et al. 2015). Although footpoint brightenings may produce wave-like disturbances propagating along quasi open field lines (Berghmans & Clette 1999), the speed of the disturbances is around 150 km s⁻¹, much higher than that of propagating knots. As waves are ubiquitous in the chromosphere, their energy will be dissipated in the chromosphere, then heat the atmosphere. We suggest that wave dissipation triggers these propagating bright knots.

Observations reveal that magnetic flux cancellation events at the stationary brightening locations are a source of mass and energy supply to the chromosphere and corona (Chitta et al. 2017; Syntelis et al. 2019). The results from previous studies and the present observations support this idea that the propagating knots are relevant to wave dissipation, and the stationary ones to magnetic reconnection. To estimate the heat energy contributed by the two kinds of bright knots respectively, several hypotheses have employed. Assuming the bright knots are spheres, the thermal energy of the bright knots can be calculated as (Tian et al. 2014)

$$E = 3 \times N_e \times k_B \times \Delta T \times V,$$

where N_e (10¹² cm⁻³) is the number density, k_B is the Boltzmann constant, and ΔT (~ 2000 K; Georgoulis et al. 2002) is the enhanced temperature of the material in the bright knots. The emission volume V can be estimated as $(4/3) \pi r^3$, with r deducing from the area of bright knots. The thermal

energy for each stationary bright knot is $\sim 5.0 \times 10^{23}$ erg, and $\sim 1.0 \times 10^{27}$ erg for 2068 stationary bright knots.

For propagating bright knots, as the enhanced brightness is weaker than that of the stationary ones, the enhanced temperature is expected to be lower. Supposing that the enhanced temperature is proportional to the enhanced brightness, ΔT is ~ 1300 K. The thermal energy for each propagating bright knot is $\sim 1.7 \times 10^{23}$ erg, and $\sim 2.7 \times 10^{26}$ erg for 1573 ones. Propagating bright knots have additional kinetic energy $(1/2)mv^2$, where $m = \rho V$ is the mass, and v is the speed. Taking $\rho \sim 10^{-12}$ g cm $^{-3}$, and $v \sim 16$ km s $^{-1}$, we obtain the kinetic energy as 6.5×10^{26} erg for all the 1573 propagating bright knots. The total energy of the propagating bright knots is 9.4×10^{26} erg, comparable to the thermal energy of the stationary bright knots. So the enhanced energy of all the bright knots is $\sim 2.0 \times 10^{27}$ erg. In the observed target, the energy loss in the chromosphere during the 3.1 hr period is 2.8×10^{30} erg. The enhanced energy of the bright knots is much less than the lost energy from the chromosphere. There are several reasons leading to the difference, e.g., many smaller or short-lifetime bright knots cannot be detected, and some bright knots are hidden by chromospheric fibrils. Additionally, the enhanced temperature may be underestimated.

In the solar corona, the thermal energy input by microflares was calculated and deduced that the heating events carried energy in the range from 8×10^{24} to 1.6×10^{26} erg (Krucker & Benz 1998). Based on a large number of small-scale brightening observations, Berghmans et al. (1998) found that the energy injected by brightenings into the solar atmosphere is inadequate for coronal heating. It has been suggested that picoflares with energies in the range 10^{21} – 10^{24} erg may heat the quiet solar atmosphere (Parnell & Jupp 2000). Similarly, Aschwanden et al. (2000) also suggested that coronal heating requires other energy carriers.

Since the power-law index α is critical to evaluate the nanoflare coronal heating model, many studies have tried to derive the power-law index of solar flare frequency distribution using various instruments and methods. For small-scale brightenings, e.g., blinkers and explosive events, the frequency distributions of ratio of peak to background intensity follow power laws (Brković et al. 2001; Winebarger et al. 2002), suggesting that small and undetectable events would release enough energy to heat the solar atmosphere. By investigating a large number of BPs, McIntosh & Gurman (2005) obtained that BP lifetime distributions are well described by modified power laws also. In this Letter, the power-law index of the stationary bright knots, as well as that of the propagating bright knots, cannot reliably be determined for two reasons. First of all, the value of the power-law slope strongly depends on the fitted range. Second, the fitted power-law range extends over less than a decade, which causes a large error in the fitted slope. This is a consequence of the incomplete sampling by visual event selection, in contrast to other distributions that are completely sampled with automated pattern recognition codes over 5 orders of magnitude (e.g., Crosby et al. 1993; Parnell et al. 2009).

As mentioned above, propagating bright knots appear in chromospheric fibrils where waves and their dissipation are ubiquitous. On the contrary, stationary knots are similar to the BPs reported before. They are detected at the footpoints of these fibrils where network magnetic fields exist, and magnetic

reconnection is suggested to produce these stationary knots (BPs). We deduce that about half of the energy for heating the chromosphere is supplied by wave dissipation, and the other half by magnetic reconnection.

The authors thank the anonymous referee for constructive suggestions and helpful comments. The observations used in this paper are obtained from the NVST and SDO teams. This work is supported by the National Natural Science Foundation of China (grant Nos. 11790304, 12073001, 11903050, 12222306, 12273060, and 11790300), Anhui Project (grant No. Z010118169), and the open topic of the Key Laboratory of Solar Activities of the Chinese Academy of Sciences (grant No. KLSA202116).

ORCID iDs

Jun Zhang  <https://orcid.org/0000-0002-1286-6931>
 Yijun Hou  <https://orcid.org/0000-0002-9534-1638>
 Feng Chen  <https://orcid.org/0000-0002-1963-5319>
 Ting Li  <https://orcid.org/0000-0001-6655-1743>
 Xiaoli Yan  <https://orcid.org/0000-0003-2891-6267>
 Yongyuan Xiang  <https://orcid.org/0000-0002-5261-6523>

References

- Abbasvand, V., Sobotka, M., Heinzel, P., et al. 2020, *ApJ*, **890**, 22
 Antolin, P., De Moortel, I., Van Doorselaere, T., & Yokoyama, T. 2017, *ApJ*, **836**, 219
 Aschwanden, M. J., Tarbell, T. D., Nightingale, R. W., et al. 2000, *ApJ*, **535**, 1047
 Aschwanden, M. J., Winebarger, A., Tsiklauri, D., & Peter, H. 2007, *ApJ*, **659**, 1673
 Berghmans, D., Auchère, F., Long, D. M., et al. 2021, *A&A*, **656**, L4
 Berghmans, D., & Clette, F. 1999, *SoPh*, **186**, 207
 Berghmans, D., Clette, F., & Moses, D. 1998, *A&A*, **336**, 1039
 Bingert, S., & Peter, H. 2011, *A&A*, **530**, A112
 Brandenburg, A., & Dobler, W. 2002, *CoPhC*, **147**, 471
 Brković, A., Solanki, S. K., & Riedi, I. 2001, *A&A*, **373**, 1056
 Chen, F., Peter, H., Bingert, S., & Cheung, M. C. M. 2014, *A&A*, **564**, A12
 Chitta, L. P., Peter, H., Solanki, S. K., et al. 2017, *ApJS*, **229**, 4
 Crosby, N. B., Aschwanden, M. J., & Dennis, B. R. 1993, *SoPh*, **143**, 275
 De Pontieu, B., Erdélyi, R., & De Moortel, I. 2005, *ApJL*, **624**, L61
 Dorotović, I., Erdélyi, R., Freij, N., Karlovský, V., & Márquez, I. 2014, *A&A*, **563**, A12
 Fang, Y., Zhang, J., Song, Z. P., Hou, Y. J., & Li, T. 2022, *A&A*, **658**, L3
 Georgoulis, M. K., Rust, D. M., Bernasconi, P. N., & Schmieder, B. 2002, *ApJ*, **575**, 506
 Gudiksen, B. V., Carlsson, M., Hansteen, V. H., et al. 2011, *A&A*, **531**, A154
 Howson, T. A., De Moortel, I., & Antolin, P. 2017, *A&A*, **602**, A74
 Jess, D. B., Reznikova, V. E., Ryans, R. S. I., et al. 2016, *NatPh*, **12**, 179
 Kholenko, E., & Cally, P. S. 2012, *ApJ*, **746**, 68
 Krishna Prasad, S., Banerjee, D., & Gupta, G. R. 2011, *A&A*, **528**, L4
 Krucker, S., & Benz, A. O. 1998, *ApJL*, **501**, L213
 Lemen, J. R., Title, A. M., Akin, D. J., et al. 2012, *SoPh*, **275**, 17
 Liu, Z., Xu, J., Gu, B.-Z., et al. 2014, *RAA*, **14**, 705
 Magyar, N., Van Doorselaere, T., & Marcu, A. 2015, *A&A*, **582**, A117
 Mandal, S., Peter, H., Chitta, L. P., et al. 2021, *A&A*, **656**, L16
 Matsumoto, T., & Suzuki, T. K. 2012, *ApJ*, **749**, 8
 McIntosh, S. W., & Gurman, J. B. 2005, *SoPh*, **228**, 285
 Morton, R. J., Verth, G., Jess, D. B., et al. 2012, *NatCo*, **3**, 1315
 Ofman, L., Knizhnik, K., Kucera, T., & Schmieder, B. 2015, *ApJ*, **813**, 124
 Parnell, C. E., DeForest, C. E., Hagenaar, H. J., et al. 2009, *ApJ*, **698**, 75
 Parnell, C. E., & Jupp, P. E. 2000, *ApJ*, **529**, 554
 Pesnell, W. D., Thompson, B. J., & Chamberlin, P. C. 2012, *SoPh*, **275**, 3
 Priest, E. R., Parnell, C. E., & Martin, S. F. 1994, *ApJ*, **427**, 459
 Ragot, B. R. 2019, *ApJ*, **887**, 42
 Rempel, M., & Cheung, M. C. M. 2014, *ApJ*, **785**, 90
 Scherrer, P. H., Schou, J., Bush, R. I., et al. 2012, *SoPh*, **275**, 207
 Shibata, K., Nakamura, T., Matsumoto, T., et al. 2007, *Sci*, **318**, 1591

- Sobotka, M., Heinzel, P., Švanda, M., et al. 2016, [ApJ](#), 826, 49
- Solanki, S. K., Lagg, A., Woch, J., Krupp, N., & Collados, M. 2003, [Natur](#), 425, 692
- Syntelis, P., Priest, E. R., & Chitta, L. P. 2019, [ApJ](#), 872, 32
- Taroyan, Y., & Erdélyi, R. 2009, [SSRv](#), 149, 229
- Terradas, J., Andries, J., Goossens, M., et al. 2008, [ApJL](#), 687, L115
- Tian, H., Kleint, L., Peter, H., et al. 2014, [ApJL](#), 790, L29
- Tomczyk, S., McIntosh, S. W., Keil, S. L., et al. 2007, [Sci](#), 317, 1192
- Vaiana, G. S., Davis, J. M., Giacconi, R., et al. 1973, [ApJL](#), 185, L47
- Vecchio, A., Cauzzi, G., Reardon, K. P., Janssen, K., & Rimmele, T. 2007, [A&A](#), 461, L1
- Winebarger, A. R., Emslie, A. G., Mariska, J. T., & Warren, H. P. 2002, [ApJ](#), 565, 1298
- Yang, S., Zhang, J., & Xiang, Y. 2015, [ApJL](#), 798, L11